

Exoplanet Observing and Characterisation

TOMAS JAMES

Abstract

For this project, the transiting extrasolar planets WASP-22 b, WASP-78 b and HATS-5 b were chosen to be observed using LCOGT telescopes in the Southern Hemisphere. The data obtained from these observations will then be used to computationally model the observed transit, allowing the calculation of orbital and physical parameters about each exoplanet. Conclusions about each planet will be compared and contrasted to the other planets observed. The parameters determined will also be compared to the known quantities for each planet.

Contents

I	Introduction	2
I	Extrasolar Planets	2
II	Detection Methods	2
III	Statistical Properties of Known Exoplanets	4
IV	LCOGT Observatories	6
II	Exoplanets for Observation	7
III	Methodology	7
I	Data Collection	7
II	Data Analysis	8
III	Aperture Photometry	8
IV	Future Work	10

I. INTRODUCTION

The discovery of the first extrasolar planet by **first** introduced a field into astronomical research that is now one of the most exciting and fast moving fields in modern astrophysics. Subsequent detections, such as the first main-sequence extrasolar planet by **MQ** continue to reveal a more diverse and rich spectrum of exoplanets. More than 20 years on from these detections, the **exo** records 1854¹ extrasolar planets that have been discovered using a variety of detection methods utilising both ground and satellite based telescopes in a multitude of collaborative missions. These vary from discovering new exoplanets to actively searching for Earth analogs that could, under the right circumstances, harbour life.

I. Extrasolar Planets

Extrasolar planets - or exoplanets - are planetary objects orbiting stars outside of the Solar System.

Since the detections made by **first** and **MQ** a multitude of dedicated projects have been launched with the primary aim of detecting and characterising exoplanets. These vary from ground-based telescopes such as WASP and HAT to spaced-based telescopes such as Kepler and CoRoT. Uniquely these missions observe a wide distribution of exoplanets, effectively allowing the formation and evolution of planetary systems to be studied.

II. Detection Methods

Extrasolar planet detection methods are divided into two classes: direct and indirect detections. A direct detection uses data that explicitly shows the presence of an extrasolar planet. An indirect detection uses effects that an extrasolar planet has on its parent star to infer the planet's existence. To date there are 5 well established detection methods. These are discussed below.

Transiting

When an exoplanet passes across the line of sight between the observer and a star, a dip in the total luminosity of the system is observed owing to the exoplanet blocking a portion of the star's flux from the observer. By plotting the total flux received as a function of time the presence of an exoplanet can be inferred if a dip in the total flux received is observed. Furthermore the dip in the total flux allows the calculation of the size of the exoplanet, as the amount of flux blocked is proportional to the exoplanet radius (**radius**). An example of this effect can be seen in Figure 1.

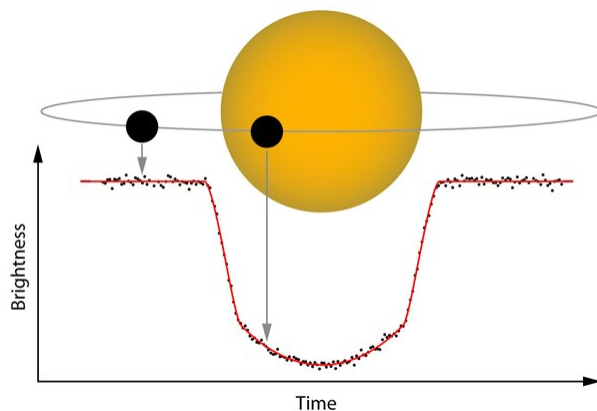


Figure 1: An example showing how the presence of an exoplanet moving across a star results in a reduction in the observed flux, as evidenced by the visible trough. (**transiting**)

¹ As of Friday 12th December 2014

This method has various limitations however. This method is biased towards finding exoplanets with large radii and small orbital periods as they block more of the star's flux incident upon the observer more often. This allows more reliable estimates of parameters like exoplanetary radius to be determined. Another limitation is that exoplanets with orbital inclinations close to 90° cannot be detected as they do not pass in front of their host star relative to the observer.

Moreover, any partially opaque object passing in front of a star will have the effect of blocking a portion of the star's total flux. **false** estimated that this is a rare occurrence, with the false positive probability (FPP)² being estimated at $< 10\%$ for almost 90% of candidates being observed by the Kepler mission.

Radial Velocity

The existence of an exoplanetary companion orbiting a host star alters the system's centre of mass causing both the exoplanet and host star to orbit about it. As a direct result of this the radial velocity of the star changes over time, peaking at a maximum when the star is moving directly toward, or away from, the observer. Conversely the radial velocity of the star is at a minimum when the star moves normal to the observer's line of sight. This is demonstrated in Figure 2.

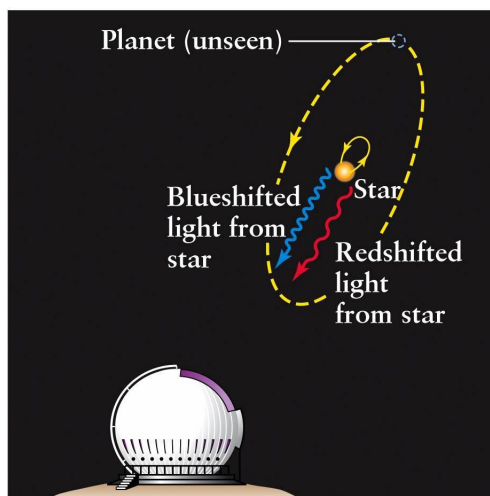


Figure 2: An example showing how the presence of a hidden exoplanet induces a change in the centre of mass of the planetary system, therefore altering the centre of orbit of each of the system's orbiting companions. This can be detected by the resulting Doppler shift of the host star's spectral lines. (**rvdetect**)

This variation is detected by observing the Doppler shift of the star's spectral lines. Whilst the star is moving towards the observer a decrease in the wavelength of the spectral lines is observed. When it is moving away from the observer an increase in the wavelength of the spectral lines is observed. No change is observed when the star is moving normal to the observer's line of sight.

This detection method is heavily biased towards large exoplanets orbiting less massive stars with small orbital periods, owing to the larger perturbation observed in the host star's orbit. However as **stats** state, the spectroscopic signature can only yield orbital parameters and a minimum mass as the orbital inclination remains unknown.

A common source of error using the radial velocity method relates to the expansion and contraction of the star itself. This produces a very similar spectroscopic signature that would be expected to be observed were the star's orbit to be perturbed by an exoplanet.

²The FPP is the probability that the exoplanet detected is a false positive, or an astronomical object passing between the telescope and the star, therefore acting as an erroneous detection.

Direct Imaging

Direct imaging detections utilise the thermal emission of an extrasolar planet to detect the planet as a source of infrared radiation in an image taken in the infrared.

The method of direct imaging is heavily biased towards large, hot planets that are separated by a large distance from their host star. This highlights a major disadvantage that direct imaging has: exoplanets lying close to a large, luminous star will be hidden owing to the large infrared luminosity difference between the two objects.

Typically this limitation is solved by the attachment of a coronagraph which blanks out the host star to avoid complications relating to its presence in the image. This is especially useful for solving problems related to the large infrared luminosity difference between a star and planet. This allows the use of longer exposure times, aiding in the potential discovery of cool exoplanets.

Microlensing

Gravitational microlensing is an effect observed in the presence of strong gravitational fields. Specifically when light interacts with a strong gravitational field it bends and undergoes magnification (**einstein**). As stated by **micro** 'in a gravitational microlensing event, a foreground lens object is detected as a result of the characteristic magnification of a background source star as it passes behind the gravitational field of the lens'. On smaller scales an increase in brightness is observed rather than magnification.

Applying this to exoplanetary detection, light from a star beyond an exoplanetary system in the observer's line of sight (the background source star) is lensed and magnified by the strong gravitational field of the system itself (the lens star). If an exoplanet is orbiting the lens star, an increase in the magnification or brightness is observed for a small duration. This anomaly can lead to the calculation of the exoplanet's mass, as well as its semi-major axis.

Projects such as OGLE are dedicated microlensing surveys that detect exoplanets using this method. This method does however require precise alignment between background and lens stars in order for any lensing to occur. Lensing events are not periodic and often rely on the random alignment of a lens and background star. As a result of this the number of detected exoplanets according to **exo** using the microlensing method is comparatively small (34) in relation to that of the radial-velocity (583) or transit methods (1163).

Pulsar Timing

Pulsar timing detections rely on the regular, periodic bursts of radio emission from an ultradense, rapidly rotating neutron star, or a pulsar.

This radio emission - owing to its stability and reliability - can be used to track the orbital period of the star. If a planetary companion is orbiting the pulsar then small orbital perturbations are to be expected owing to the orbit of the system about a common centre of mass. This results in periodic anomalies in the detection of the emitted radio signal as the star moves around the centre of mass of the system. Tracking these anomalies allows the period of the star to be determined and crucially, the mass and orbital parameters of the exoplanet as well.

The reliability and accuracy of the pulsar timing method allows much smaller exoplanets to be detected. The first discovered exoplanet was found orbiting the pulsar PSR1257+12 by **first** in 1992. According to the **exo** however only 18 exoplanets have been detected using this method since 1992, indicating that exoplanets orbiting pulsars are rare occurrences.

III. Statistical Properties of Known Exoplanets

To better understand the orbital behaviour of exoplanets, along with their calculated properties, graphs that could potentially reveal trends were plotted. This was achieved by using the **exo** to download³ data on all detected exoplanets. A Python script was written to process this data with the primary aim of reducing it the required graphs.

³The last download of this data was 12th December 2014

Period and Semi-Major Axis

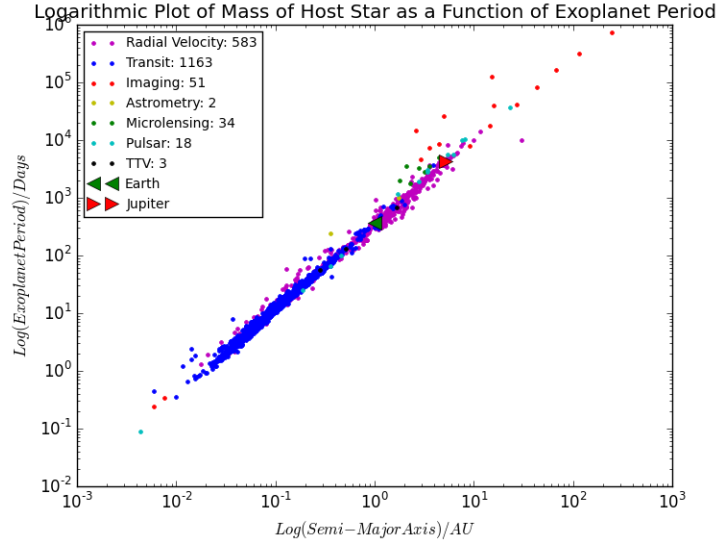


Figure 3: A loglog plot showing the relationship between an exoplanet's period and its semi-major axis.

As can be seen in Figure 3 the loglog plot of orbital period vs semi-major axis produces a very well defined and characteristic straight line. Kepler's 3rd Law relates period and semi-major axis as defined in equation 1.

$$T^2 \propto a^3 \quad (1)$$

In this instance T is the orbital period and a is the semi-major axis. Given that orbital systems are bound by Kepler's Laws (the Jupiter and Earth points confirm that this is the case for those 2 Solar System planets) the shape of the graph is to be expected. Interestingly a number of points lie off the main sequence of data in Figure 3. Regrettably the **exo** does not include error estimations for all exoplanet entries, meaning firm conclusions about why these points lie off of the main sequence cannot be drawn without speculation.

Figure 3 also allows analysis of the sensitivity of each detection method. For example the exoplanet with the fastest orbital period and smallest semi-major axis was detected using the pulsar timing method, whilst the exoplanet with the slowest period and largest semi-major axis was detected using the direct imaging method. Direct imaging does however detect exoplanets across the most diverse range of periods and semi-major axes of those detection methods considered, ranging from the second-smallest semi-major axis to the largest.

Furthermore Figure 3 shows that nearly all exoplanets detected using the transit method orbit at <1 AU with orbital periods <365 days. This shows graphically the bias towards small semi-major axis and short period. Very few exoplanets are observed with orbital characteristics in excess of Jupiter (a semi-major axis >5.2 AU and period >4332 days). The aforementioned bias and minimal detections using methods that are capable of detecting exoplanets with larger semi-major axes and longer period mean the existence of exoplanets at these orbital parameters cannot be dismissed.

Mass-Radius Relationship

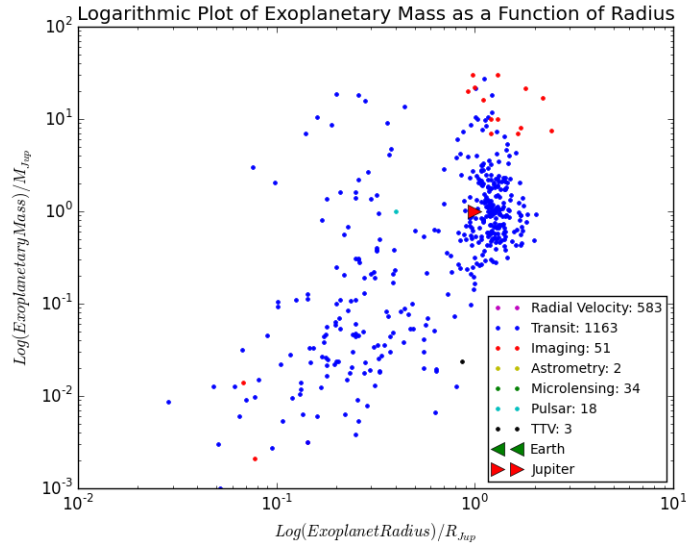


Figure 4: A loglog plot showing the relationship between an exoplanet's mass and its radius.

Considering Figure 4, a general trend is observed showing that mass is correlated with radius. Mass and radius are linked through equation 2.

$$m = \frac{4}{3}\pi R^3 \rho \quad (2)$$

where m is the planetary mass, R is the planetary radius and ρ is the planetary density. If equation 2 describes the profile shown in Figure 4, then the deviation from constant positive correlation is due to ρ varying (i.e. ρ is not constant across all exoplanets). This behaviour is observed in the Solar System, as the calculated densities vary for all Solar System planets. For density to be calculated however both the precise mass and radius need to be known. As a result both the radial velocity and transit detection methods need be used in order to determine these quantities reliably.

Interestingly a grouping of data points exists close the $1 R_{Jup}$ marker, indicating a large number of exoplanets having a radius close to this value. Jupiter like exoplanets are not uncommon. As stated by **stats** the limitations in observation techniques lend themselves to detecting Jupiter like planets. Whilst this grouping has a narrow spread of radii close to the $1 R_{Jup}$, its associated mass is spread over a much larger range, indicating non-uniform density.

Figure 4 also highlights how dominant the transit detection method is, having twice the number of confirmed detections than all other detection methods combined. It also confirms that the transit method can detect exoplanets across the largest mass range. Both Figures 3 and 4 follow confirmed mathematical trends and show that the Solar System isn't an anomalous planetary system.

IV. LCOGT Observatories

Observations were limited to LCOGT sites in the Southern Hemisphere owing to a greater number of available telescopes. These sites are listed in Table 1.

Observatory	Latitude (Deg)	Longitude (Deg)
Cerro Tololo	30° 10' 2.64"S	70° 48' 17.28"W
Sutherland	32° 22' 48"S	20° 48' 36"E
Siding Spring	31° 16' 23.88"S	149° 4' 15.6"E

Table 1: A table showing the observatories housing LCOGT telescopes that were used for data collection during this project (**sites**).

As all of the sites in Table 1 house 1.0m Ritchey-Chretien Cassegrain telescopes, it was this variety of instrument that was used to collect data. Of all of these sites however, Siding Spring is the only telescope to currently have both a 2.0m and 1.0m Ritchey-Chretien variant.

Each 1.0m telescope allows for the selection of 2 different sensors, along with a range of filters (**1m**).

- SBIG STX-16803, FOV 16x16 arcmin
- Sinistro Fairchild CCD-486 BI, FOV 27x27 arcmin

Whilst it would have been preferable to use one sensor across all observations and observatories, not all observatories in the Southern Hemisphere use the same sensor. Both Sutherland and Siding Spring operate using the SBIG sensor whilst Cerro Tololo uses the Sinistro sensor.

II. EXOPLANETS FOR OBSERVATION

Observations were required to be obtained during the time frame October 2014 - December 2014. To determine which exoplanets were visible during this period, the STARALT tool (**staralt**) was used in conjunction with the Exoplanet Transit Database (**etd**). Only transiting exoplanets were considered for this project as equipment required for other detection methods was not available at the observatories used.

Once the number of visible sources was determined, the number of those sources that were undergoing visible transits during the required time period was determined using the ETD's Transit Prediction function. These were crossreferenced using the STARALT function STARMULT, which produces an optimal observing date for a given source based on the observatory coordinates in Table 1 and stipulation that observations must occur above an altitude of 30° above the horizon^{footnote}The airmass below this altitude would have rendered any observations highly prone to errors from atmospheric effects. The candidates for observation can be seen in Table 2.

Exoplanet	RA	Dec	Date
WASP-22 b	03h 31m 16.3s	-23° 49' 11"	09/11/2014
WASP-78 b	04h 15m 02.0s	-22° 06' 59.1"	30/11/2014
HATS-5 b	04h 28m 53.47s	-21° 28' 54.0"	01/12/2014

Table 2: A table showing the exoplanets to be observed in this project along with the proposed date of observation and the coordinates, in RA/Dec, of each source (**etd**).

III. METHODOLOGY

I. Data Collection

In order to determine the best exposure times for each candidate, initial test exposures were assigned to each system - these test exposures varied in 10s integration time increments from 30s - 90s. The resulting files were then assessed manually to determine the quality of the data and subsequently the best integration time.

This process determined that 90s exposures for all systems generated the best quality data. A longer exposure time is preferable in order to maximise the SNR⁴.

For an exoplanet to be characterised it is necessary to observe the system as many times as possible over the duration of the transit. A baseline flux outside of the transit is also needed in order for the transit itself to be visible, so exposures were started 15 minutes before the estimated transit start (i.e. 15 minutes before the planet first occults the host star) and concluded 15 minutes after the transit ended. The optimum number of exposures was calculated using equation 3.

$$N_e = \frac{D_{transit} + 2t_{window}}{t_e + t_{read}} \quad (3)$$

In equation 3, N_e is the maximum number of exposures, $D_{transit}$ is the transit duration in seconds, t_{window} is the time between observations beginning and transit beginning, t_e is the exposure time in seconds and t_{read} is the necessary readout time for the telescope in use. In this case, $t_{window} = 900s$ and $t_{read} = 15s$.

Whilst N_e is the theoretical maximum number of exposures possible, this was reduced by a relative number of exposures to allow the telescope in use to prepare for the next exposure in ample time.

LCOGT's online scheduler was used to insert the observation requests into the observation queue.

II. Data Analysis

LCOGT systems use data reduction pipelines based upon the ORAC-DR infrastructure developed by **orac-dr** for UKIRT and JCMT initiatives. The pipeline reducing data from the LCOGT system runs multiple independent recipes for bad-pixel masking, bias subtraction, flat field correction and WCS fitting (**pipeline**).

The resulting pipeline reduced and corrected data was then downloaded from the LCOGT Data Archive and analysed. In the case of this project the primary form of data analysis comprised of aperture photometry using the GAIA package, available as part of the Starlink Project (**starlink**).

III. Aperture Photometry

Photometry is a technique for measuring an object's incident radiation flux. Measurements made with this method can be used to calculate that object's luminosity and/or magnitude.

To perform aperture photometry using GAIA, the data (in the form a .FITS file) was loaded and a circular aperture was placed over the object to be analysed. Initially GAIA sums all object data counts within the aperture. In this analyses a seperate, independent circular background aperture was used in order to capture a sky area. This was used as it eliminated any stray flux from the object that may contaminate the background count. The incident flux is then calculated by $F_i = F_{o+b} - F_b$ where F_i is the incident flux from the object alone, F_{o+b} is the flux incident from the object and background and F_b is the flux from the background alone.

⁴SNR $\propto \sqrt{t}$ where t is the integration time

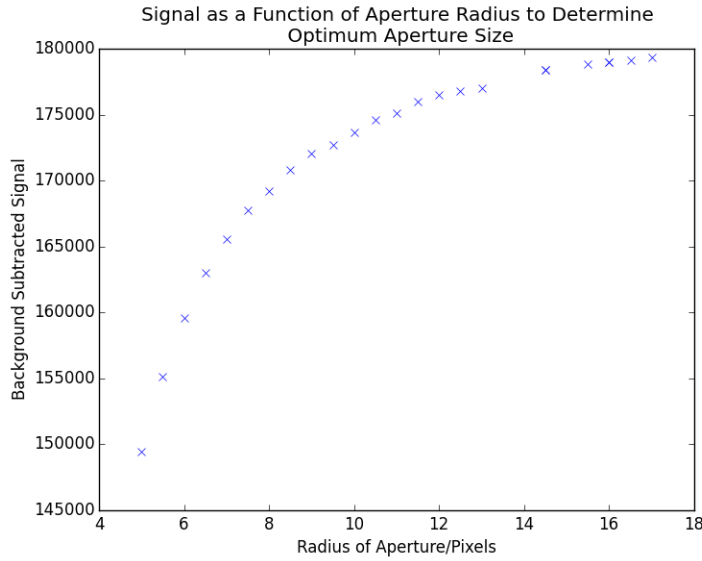


Figure 5: An example of how the optimum aperture size was determined by observing how the background subtracted signal varies with aperture size. The point at which the gradient of the curve becomes constant - in this instance at the 12 pixel point - is the optimum aperture size.

The required aperture size varies with the luminosity of the star in question, along with its radius. An aperture that is too small will not capture all of the star's flux and indeed an aperture that is too large will collect a larger portion of the background flux. To determine the optimum aperture size it was decided to perform aperture photometry on the star with a variety of different aperture sizes. The resulting background subtracted count was then plotted against the aperture size to assess how the count varied with aperture radius. An example for Qatar-1 b, provided by project supervisor Dr. E Gomez, is seen in Figure 5.

As the aperture size increases, so does the measured count inside of the aperture. When all of the star's flux has been measured, any further increase in aperture size will detect a uniform, constant background leading to a constant increase in the count. This is manifested graphically by a constant gradient. The point at which the graph plateaus is the optimum aperture size.

For a transit to be reliably characterised differential aperture photometry is performed in addition to the above using equation 4.

$$S = \frac{F_i}{F_c - F_b} \quad (4)$$

In equation 4, S is the calibrated flux, F_i is the incident flux as defined earlier, F_c is the calibration star flux and F_b is the background flux.

This essentially calibrates the flux from the object of interest against another object of similar brightness in the field of view. Providing that the calibration star has constant luminosity (and therefore constant flux) this normalises the count in order to account for any atmospheric effects between frames. For reliability this is performed with as many different calibration stars as the field of view allows.

This procedure is repeated across an even number of exposures, evenly distributed across the transit and, importantly, about its transit centre. A Python script was then written to plot S as a function of time, thereby producing a light curve.

IV. Modelling the Transit

IV. RESULTS

V. FUTURE WORK